

Revision 4

Word count: 3530

1 **Single-crystal X-ray diffraction of fluorapatite to 61 GPa**

2 Melinda J. Rucks¹, Gregory J. Finkelstein¹, Dongzhou Zhang^{2,3}, Przemyslaw K. Dera^{2,3},

3 and Thomas S. Duffy¹

4 ¹Department of Geosciences, Princeton University, Princeton, New Jersey 08544, U.S.A.

5 ²Hawaii Institute of Geophysics & Planetology, School of Ocean and Earth Science and
6 Technology, University of Hawaii, Honolulu, Hawaii 96822, U.S.A.

7 ³GSECARS, University of Chicago, Building 434A, 9700 South Cass Avenue, Argonne, Illinois
8 60439, U.S.A.

9

10 **Abstract**

11 Apatite is a mineral of widespread importance in Earth and planetary science. Here we
12 examine the behavior of a natural fluorapatite (FAP) crystal from Durango (Mexico) under
13 compression to 61 GPa. Single-crystal X-ray diffraction experiments were carried out in a
14 diamond anvil cell using a synchrotron source. The apatite structure persists up to 32.4 GPa.
15 Birch-Murnaghan equation of state parameters were fit to the pressure-volume data for
16 fluorapatite for two cases: fixing V_0 at its measured ambient value resulted in a bulk modulus,
17 K_{0T} , of 97.0(8) GPa and a pressure derivative of the bulk modulus, K'_{0T} , of 3.3(1), while fixing V_0
18 and K_{0T} at its ambient value 90.5 GPa (derived from ultrasonically measured elastic constants)
19 resulted in a K'_{0T} value of 4.1(1). At 35.6 GPa, fluorapatite transforms to a triclinic phase ($P-I$
20 **{note to typesetting, these minus signs are overbars on top of the 1.}**, $Z=4$), designated here
21 as fluorapatite II (FAP-II). This phase persists up to at least 61 GPa. The major structural
22 differences between FAP and FAP-II involve the buckling of the Ca polyhedra along the c -axis
23 and changes in the number and coordination of the Ca sites. Our study extends the pressure range

Revision 4

Word count: 3530

24 over which fluorapatite has been examined by more than a factor of three, providing new insights
25 into its structural response to high-pressure conditions.

26 INTRODUCTION

27 Apatite, $\text{Ca}_5(\text{PO}_4)_3(\text{F}, \text{Cl}, \text{OH})$, occurs widely in rocky bodies in the solar system, playing
28 an important role as a host for phosphorous and other volatiles. It is one of the most prevalent
29 volatile-bearing phases observed in lunar samples (McCubbin et al. 2010, 2011; Boyce et al.
30 2014; McCubbin and Jones 2015), and is also found in meteorites (Chen et al. 1995; Sarafian et
31 al. 2013). The apatite structure is highly adaptable and has the ability to incorporate several
32 cations and anions including Sr^{2+} , Mn^{2+} , Pb^{2+} , Br^- , CO_3^{2-} , and rare earth elements (Hughes and
33 Rakovan 2015). Recently, there has been growing interest in the use of apatite as a diagnostic of
34 shock metamorphism in meteorites and at impact sites (Cox et al. 2020; Kenny et al. 2020). This
35 highlights the need for detailed characterization of the behavior of apatite minerals under static
36 and dynamic compression.

37 Fluorapatite (FAp), $\text{Ca}_5(\text{PO}_4)_3\text{F}$, crystallizes in the hexagonal system (space group $P6_3/m$,
38 $Z=2$) at ambient conditions (Figure 1). The structure contains two types of Ca polyhedra,
39 designated Ca1 and Ca2. The Ca1 polyhedron is a tricapped trigonal prism with nine-fold
40 coordination. The Ca1 polyhedra share (001) faces and form chains parallel to the c -axis. The
41 cations in Ca2 are enclosed in an irregular seven-coordinated polyhedron with six oxygen bonds
42 and one fluorine bond. PO_4 tetrahedra link adjacent Ca1 and Ca2 polyhedra (White and Dong
43 2003; White et al. 2005). The F anions are located in channels running along the c -axis. The
44 cations in the Ca2 polyhedra define a triangle with an F anion at its center with fractional

Revision 4

Word count: 3530

45 coordinates (0, 0, 1/4). Detailed descriptions of the FAp structure can be found elsewhere (White
46 et al. 2005; Hughes and Rakovan 2015).

47 The structure and properties of natural apatites have been the subject of extensive study
48 (Hughes 2015; Hughes and Rakovan 2015). An area of interest has centered around the effects of
49 substitution of anions that reside in the halogen site, and how solid solution affects the site
50 location (Murayama et al. 1986; Hughes et al. 1989, 2014). A number of studies have also been
51 conducted to characterize apatite's structural behavior and phase stability at high pressure
52 (Brunet et al. 1999; Comodi et al. 2001; Matsukage et al. 2004; Konzett and Frost 2009; Konzett
53 et al. 2012; Cámara et al. 2018). Previous studies have shown that fluorapatite persists to 18.3
54 GPa at room temperature, but decomposes into an assemblage containing tuite, $\gamma\text{-Ca}_3(\text{PO}_4)_2$, at
55 ~ 12 GPa and temperatures above 1000°C (Sugiyama and Tokonami 1987; Matsukage et al.
56 2004). Natural tuite has been observed in melt veins of shocked meteorites (Baziotis et al. 2013;
57 Xie et al. 2013). In order to better understand its structural response to compression, we have
58 examined apatite to 61 GPa at ambient temperature using synchrotron-based single-crystal X-ray
59 diffraction techniques.

60 **EXPERIMENTAL METHODS**

61 A natural, gem-quality crystal of fluorapatite from Cerro de Mercado, Durango, Mexico
62 (Excalibur Minerals) was used in this study. Single-crystal X-ray diffraction at ambient
63 conditions yielded lattice parameters and a unit cell volume of $a = 9.3937(4)$ Å, $c = 6.8821(3)$ Å,
64 $V = 525.93(5)$ Å³, where the numbers in parentheses are one standard deviation uncertainties.
65 Microprobe analysis yielded a composition of $(\text{Ca}_{5.05}\text{Na}_{0.04})(\text{P}_{2.93}\text{Si}_{0.03}\text{S}_{0.02}\text{O}_4)_3(\text{F}_{0.88}\text{Cl}_{0.06}\text{OH}_{0.04})$,
66 see Supplementary Table 1. These are in agreement with literature values for Durango apatite

Revision 4

Word count: 3530

67 (Hughes et al. 1989; Schouwink et al. 2010; Hovis et al. 2014, 2015). A comparison of unit cell
68 parameters for the Durango apatite used in this study and other fluorapatite samples is shown in
69 Supplementary Table 2. A Raman spectrum of the starting material is shown in Supplementary
70 Figure 1.

71 A crystal fragment with approximate dimensions $0.018 \times 0.018 \times 0.008 \text{ mm}^3$ was
72 selected and loaded into a diamond anvil cell (DAC). The cell incorporated 300- μm diameter
73 culet diamonds backed by Boehler-Almax-type seats with a 70° conical opening (Boehler and De
74 Hantsetters 2004). A sample chamber was created by drilling a $\sim 170\text{-}\mu\text{m}$ hole in a rhenium
75 gasket pre-indented to a thickness of $\sim 33 \mu\text{m}$. Two ruby spheres and a fragment of Au foil were
76 included in the sample chamber as pressure calibrants. Helium was loaded into the cell as a
77 pressure transmitting medium using the GSECARS high-pressure gas loading system (Rivers et
78 al. 2008).

79 Single-crystal X-ray diffraction experiments at both ambient and high pressure were
80 conducted at the 13-BM-C (PX²) beamline of the GSECARS sector of the Advanced Photon
81 Source, Argonne National Laboratory (Zhang et al. 2017). Ambient measurements were
82 conducted at the same beamline, outside the DAC on a separate crystal from the same source as
83 the sample used for the high-pressure experiments. The sample was compressed in $\sim 3 \text{ GPa}$ steps
84 using a gas membrane drive. At each compression step, X-ray diffraction data were collected
85 over a 65° angular range along a single rotation axis with a $\frac{1}{4}$ -degree step size, and 1-s exposure
86 time per frame. The wavelength of the incident X-ray was 0.4343 \AA . The sample-to-detector
87 distance and, the orientation of the detector were calibrated using an LaB_6 standard. The data
88 were analyzed using the Bruker APEX3 software. The raw data were processed and integrated
89 using a dynamic mask algorithm to mask blank regions in the Pilatus detector. Absorption

Revision 4

Word count: 3530

90 corrections were conducted through a scaling step after integration using the SADABS software
91 package. The structure was then solved using SHELXT and refined using the APEX3 refine
92 plug-in based on the ShelXLe engine (Hübschle et al. 2011; Sheldrick 2014). Structure
93 refinements were carried out for all pressures up to 25.8 GPa, and at 43.4 GPa. Anisotropic
94 atomic displacements were used for all but the highest pressure. CIF files are provided in
95 supplementary material. Representative data for an hk0 precession image are shown in
96 Supplementary Fig. 2. Ruby fluorescence spectra and Au powder X-ray diffraction patterns were
97 collected before and after the single-crystal diffraction collection at each compression step.
98 Pressures were determined using the [111] reflection of gold using the pressure scale of (Fei et
99 al. 2007). The pressures from ruby fluorescence (Mao et al. 1986; Shen et al. 2020) were
100 generally within 1 GPa of the gold values. The ruby lines remained sharp and well separated to
101 maximum pressure, indicating minimal non-hydrostatic stresses.

102 After reaching the maximum pressure of 61 GPa, the cell was decompressed to 43.4 GPa
103 and removed from the membrane drive to facilitate the collection of additional data for structure
104 refinement. Data were collected at this pressure in phi-scans, for ω values of 0 and 180 degrees
105 at each of three χ positions (-45° , 0° , and 45°). The data collection in this case was performed
106 over a 67° angular range on a single rotation axis with a $\frac{1}{4}$ -degree step size, and 2-s exposure
107 time. The structure at this pressure was solved and refined as described above, except that due to
108 limitations in reciprocal space coverage, atomic positions were refined isotropically.
109 Visualization and analysis of the refined structures was carried out using the software
110 CrystalMaker (Palmer 2015).

111 **RESULTS**

Revision 4

Word count: 3530

112 Analysis of the X-ray diffraction data showed that fluorapatite persists in the $P6_3/m$
113 structure up to 32.4 GPa at room temperature. This is consistent with previous results from
114 powder X-ray diffraction to 18.3 GPa (Brunet et al. 1999) and Raman spectroscopy to 25 GPa
115 (Williams and Knittle 1996). Representative structure refinements at selected pressures are
116 shown in Table 1. Our results are consistent with previous structure refinements both at ambient
117 and high pressure (Young et al. 1969; Sudarsanan and Young 1978; Hughes et al. 1989; Comodi
118 et al. 2001). It should be noted that for the two compression steps above 25.8 GPa, there was a
119 decrease in the quality of the refinements, as the crystallographic R factor ($R1$) increased to
120 0.159 at 32.4 GPa relative to the value of 0.036 at 25.8 GPa (Table 1). This is likely due to an
121 increase of crystal mosaicity in this pressure range.

122 The variation of the unit cell parameters with pressure for fluorapatite is given in Figure 2
123 and Table 2. At low pressures, the variation of the axial lengths is in agreement with an earlier
124 single-crystal study on synthetic fluorapatite (Comodi et al. 2001) (Fig. 2). A linearized Birch-
125 Murnaghan equation was fit to the axial compression data (Xia et al. 1998) (Figs. 2 and 3). The
126 resulting axial moduli, K_{0a} and K_{0c} , and their corresponding pressure derivatives, K'_{0a} and K'_{0c}
127 were: $K_{0a} = 82.5(4)$ GPa, $K'_{0a} = 3.80(5)$, $K_{0c} = 141.5(9)$ GPa, and $K'_{0c} = 1.77(8)$. These results
128 indicate that the a -axis is initially much more compressible than the c -axis but the axial
129 compressibilities converge by 25 GPa. This is a consequence of the stiffness of the polyhedral
130 chains along the c -axis relative to the compressibility of the anion channels perpendicular to c
131 (Sha et al. 1994; Comodi et al. 2001) (Fig. 3). As a result of the differences in axial
132 compressibility, the c/a ratio initially increases with pressure (Fig. 4), in agreement with previous
133 studies on both single-crystal and polycrystalline samples (Brunet et al. 1999; Comodi et al.

Revision 4

Word count: 3530

134 2001; Matsukage et al. 2004). Above ~15 GPa, the c/a ratio flattens with pressure as the axial
135 compressibilities converge.

136 The volume compression data were fit with a 3rd order Burch-Murnaghan equation of
137 state using the EOSfit7c software (Angel et al. 2014). By fixing the ambient volume, V_0 , we
138 obtain an isothermal bulk modulus, K_{OT} , of 95.8(4) GPa and a pressure derivative of the bulk
139 modulus, K'_{OT} , of 3.4(1) (Fig. 5). We also performed the fitting by fixing $K_{OT} = 90.5$ GPa, which
140 is taken from single-crystal elastic constant measurements (Sha et al 1994), corrected from
141 adiabatic to isothermal conditions. In this case we obtain $K'_{OT} = 4.1(1)$. The two equations of
142 state provide nearly identical fits to the data. When fit to a second order Birch-Murnaghan
143 equation the resulting bulk modulus was $K_{OT} = 92.3(5)$ GPa. The variation of unit cell volume
144 with pressure in our study is generally in agreement with earlier studies to about 10 GPa (Brunet
145 et al. 1999; Comodi et al. 2001; Matsukage et al. 2004), with deviations at higher pressures,
146 likely due to the presence of non-hydrostatic stress in earlier work on polycrystalline samples
147 (Brunet et al. 1999) (Figure 5). A comparison of our equation of state results with other studies is
148 given in Table 3.

149 At 35.6 GPa, a change in the diffraction pattern was observed, indicating a phase
150 transition to a new structure (designated here as FAp-II). The new phase persisted upon
151 subsequent compression to the maximum pressure reached of 61 GPa. The diffraction data could
152 be fit to a triclinic unit cell (Table 4), but the diamond anvil cell and associated membrane drive
153 configuration provided insufficient reciprocal space coverage for a refinement of this low-
154 symmetry structure. Consequently, as described in the methods section, after decompressing the
155 cell to 43.4 GPa and removing it from the membrane drive, data were collected at additional χ
156 rotations. This made it possible to perform a structure refinement at this pressure indicating a

Revision 4
Word count: 3530

157 space group of $P-1$ **{note to typesetting, these minus signs are overbars on top of the 1.}**
158 ($Z=4$), which yielded an R1 value of 0.0537 (Supplementary Table 3).

159 In the FAp-II structure, there are ten Ca sites. These sites can be grouped into two sets
160 that are related to the Ca1 and Ca2 sites in FAp. For simplicity, we refer to these groups of sites
161 as Ca1' (Ca1A, Ca1B, Ca1C, and Ca1D) and Ca2' (Ca2A, Ca2B, Ca2C, Ca2D, Ca2E, Ca2F),
162 respectively. In the case of Ca1', there are four sites, two of which are 8-coordinated (Ca1C and
163 Ca1D) and two are 9-coordinated (Ca1A and Ca1B), which form a column in an 8-8-9-9
164 arrangement, sharing faces similar to the Ca1 column in the FAp phase. The Ca1' polyhedral
165 columns are connected through edge and corner sharing with PO_4 tetrahedra (Fig. 6).

166 In the case of Ca2', there are six unique sites, two forming 8-coordinated polyhedra
167 (Ca2A and Ca2B) and four forming 9-coordinated polyhedra (Ca2C, Ca2D, Ca2E, and Ca2F).
168 As in the FAp structure, the Ca2' cations form layers of Ca2' site triangles with a central column
169 of F ion sites. In the FAp structure, the Ca2 triangles are translated through a 180° screw axis
170 along the c-axis. This relationship is generally retained in the FAp-II structure, even though the
171 screw axis is absent in the $P-1$ **{note to typesetting, these minus signs are overbars on top of**
172 **the 1.}** space group. There are two unique Ca2' layers, designated here as X and Y, where X is
173 composed of 9 coordinated sites and Y is a combination of two 8-coordinated sites and one 9-
174 coordinated site (Figs. 6 and 7). The ideal F^- anion sites, of which there are 3 in the FAp-II
175 structure ((F1A, F1B, and F1C)), are vertically offset such that they appear between the Ca2'
176 triangle layers. The Ca2' columns follow a X – F1B – X' – F1C – Y – F1A – Y' – F1C
177 arrangement, where X' and Y' are the inverse of X and Y (Fig. 7), similar to the screw axis
178 present in the low-pressure structure. In the FAp structure, the Ca2 sites form columns through
179 corner sharing of the Ca2 polyhedra; in contrast in FAp-II these Ca2' polyhedral are connected

Revision 4
Word count: 3530

180 through a combination of face and edge sharing. Ca2' sites that are 9-coordinated are face shared
181 with other 9-coordinated Ca2' sites and the Ca2' sites that are 8-coordinated are all edge shared
182 with surrounding Ca2' polyhedral except for one face, which is shared with a Ca2' site that is 9-
183 coordinated.

184 A 3rd order Burch-Murnaghan equation of state was fit to the volume compression data
185 for FAp-II (Fig. 8). The high-pressure data were fit by fixing the K'_{0T} to the value of 4.1 value
186 obtained from the fits of the FAp structure. The resulting ambient unit cell volume (V_0) and
187 isothermal bulk modulus (K_{0T}) fit parameters are 258(9) Å³ and 97(19) GPa, respectively (see
188 also. Table 3). There is thus little change in the compressibility between the low- and high-
189 pressure phases.

190 **Discussion and Implications**

191 Fluorapatite is the most abundant phosphate mineral and has widespread importance in
192 geology. It is a member of the apatite supergroup, a chemically and structurally diverse set of
193 compounds with many important technological applications. An understanding of apatite under
194 compression is of growing interest in light of the increased use of apatite as a diagnostic of
195 impact events. Most previous compression studies of apatites are restricted to relatively low
196 pressures or polycrystalline material and little is known about how the structure of this mineral
197 or phosphates more generally respond when subjected to more extreme pressures. Our study
198 thus provides new insights into the structural response of fluorapatite as interatomic distances are
199 reduced.

200 Figure 9 shows the variation in average Ca1-O and Ca2-O bond lengths with
201 compression in FAp. The Ca2 polyhedra become more regular with compression as the

Revision 4

Word count: 3530

202 relatively long Ca2-O1 bond is highly compressible and becomes similar in length to the Ca2-
203 O3' bond at 25.8 GPa. Comodi et al., (2001) suggests that the Ca1 polyhedra become more
204 regular with pressure, however, here we observe the opposite whereby the mean Ca1-O bond
205 distance decreases from 2.554 Å at 1 bar to 2.432 Å at 25.8 GPa, but the standard deviation of
206 the bond distances increases from 0.18 Å to 0.23 Å. The bond distances in the PO₄ tetrahedra
207 change little with pressure as expected.

208 A useful metric for understanding the distortion of apatite structures is the metaprism
209 twist angle (ϕ). The fluorapatite structure can be described in terms of a triangular network of
210 oxygen anions, where the Ca1 site involves regular triangles of O1 and O2 which twist to form
211 these metaprisms (White and Dong 2003; White et al. 2005; Baikie et al. 2007). The twist angle
212 between these O²⁻ triangles can be related to compositional effects (Dong and White 2004a,
213 2004b; Baikie et al. 2007). Our data at ambient pressure are consistent with typical fluorapatites,
214 which yield $\phi = 23.3^\circ$. Upon compression to 25.8 GPa, we observe an increase in twist angle to
215 23.9° . We can characterize the distortion of the high-pressure structure through the twist angle of
216 the FAp-II oxygen metaprisms identified as equivalent to those in FAp. The average twist angle
217 for the 8- and 9- coordinated Ca1' sites are 28.7° and 18.9° , respectively. As discussed in Brunet
218 et al. (1999), the higher twist angles may be correlated with higher stiffness. The large difference
219 in twist angle suggests that in FAP-II the 9-coordinated Ca1' sites may be more compressible
220 than the 8-coordinated sites.

221 In end-member fluorapatite, the F anions are in columns along the *c*-axis, located on
222 mirror planes and residing at the center of a triangle defined by three surrounding Ca cations. In
223 natural fluorapatites such as the Durango sample used here, the presence of minor amounts of Cl⁻
224 and OH⁻ substituting for F⁻ complicates the picture. These ions do not fit well in the center of the

Revision 4

Word count: 3530

225 Ca triangle and so adopt off-mirror positions along the channel axis. This positional shift can in
226 turn displace nearby fluorine ions, leading to the possibility of multiple partially occupied
227 channel anion positions (Hughes et al 2014).

228 In our refinements, we assumed an end-member fluorapatite composition as we cannot
229 resolve the presence of minor amounts of other anions. At lower pressures, our results are
230 consistent with the F anion on or near the mirror plane consistent with earlier work (Comodi et
231 al. 2001). However, at pressures above 10 GPa, we observe a strongly increasing elongation of
232 the atomic displacement parameter associated with this site. An important feature of the high-
233 pressure behavior of apatite is the high compressibility of the anion channels normal to the *c*-
234 axis. As a result, the area defined by the Ca triangle decreases strongly with pressure and is
235 reduced by about 25% at 25.8 GPa relative to its ambient value. We postulate that reduction of
236 the size of the channel with pressure may further drive the F anions away from their ideal
237 position along the *c*-axis. These changes will also lead to corresponding effects on the
238 electrostatic interactions between neighboring channel anions as well as with the surrounding
239 cations under compression. The result would likely be multiple anion positions or disordering
240 that produce the observed large anisotropic displacements and preclude refining the positions as
241 separate sites. Further work is required to better constrain the behavior of the F anion at high
242 pressure.

243 As far as we are aware, the FAp-II phase is the first report of a triclinic apatite formed
244 under compression. Low-symmetry structures occur in apatites that incorporate cations with
245 relatively large ionic radii into both the polyhedral and tetrahedral sites (White et al. 2005). The
246 transformation from FAp to FAp-II involves collapse along the *c*-axis, as the Ca1 and Ca2
247 columns can no longer compress without deforming through twisting and buckling of these sites

Revision 4
Word count: 3530

248 away from the *c*-axis, resulting in the triclinic structure. As can be seen in the structure models
249 (Fig. 6), pseudo-hexagonal symmetry is retained in the triclinic structure. Additionally, as in the
250 FAp structure, we observe disorder of the F⁻ site (Fig. 7). Two of the three unique F sites are
251 disordered with half occupancy, though our interpretation of these sites is limited as we were
252 unable to achieve refinement of the anisotropic displacement parameters as discussed above.

253 A major difference between the FAp and FAp-II structures is the change in coordination
254 of the Ca sites. The overall oxygen arrangement around the Ca1/Ca1' are similar between the
255 FAp and FAp-II structures (Supplementary Figure 3). The three O1 and three O2 oxygens are
256 involved in the face sharing of the Ca1/Ca1' cation polyhedra. In the FAp structure, the Ca1 site
257 has three additional bonds to O3. The decrease in coordination across the phase transition is due
258 to both the kinking away from the *c*-axis shifting of the Ca1 site and distortion of the position
259 and orientation of the PO₄ tetrahedra. These movements pull one oxygen away from the Ca1 site
260 and it is captured by Ca2 site, changing the coordination of Ca1 from 9- to a combination of 8-
261 and 9-coordinated polyhedra. Additionally, the coordination of the Ca2 site increases from 7 to 8
262 or 9 in the high-pressure phase.

263

264 **DATA AVAILABILITY**

265 Structure data (.cif files) presented here is publicly available at the Princeton University
266 DataSpace repository under the following link <https://doi.org/10.34770/ark9-b372>.

267 **ACKNOWLEDGMENTS**

268 We thank Sergey Tkachev for assistance with gas loading, and Celine Martin for assistance with
269 microprobe data collection at the American Museum of Natural History. This work was

Revision 4
Word count: 3530

270 supported by the Department of Energy/National Nuclear Security Agency under Cooperative
271 Agreement DE-NA0003957. GeoSoilEnviroCARS is supported by the NSF and the Department
272 of Energy (DOE). Use of the gas loading system was supported by COMPRES and GSECARS.
273 This research used resources of the Advanced Photon Source, a DOE User Facility operated by
274 Argonne National Laboratory.

275 REFERENCES CITED

- 276 Angel, R.J., Alvaro, M., and Gonzalez-Platas, J. (2014) EosFit7c and a Fortran module (library)
277 for equation of state calculations. *Zeitschrift für Kristallographie - Crystalline Materials*,
278 229.
- 279 Baikie, T., Mercier, P.H.J., Elcombe, M.M., Kim, J.Y., Le Page, Y., Mitchell, L.D., White, T.J.,
280 and Whitfield, P.S. (2007) Triclinic apatites. *Acta Crystallographica*, B63, 251–256.
- 281 Baziotis, I.P., Liu, Y., DeCarli, P.S., Jay Melosh, H., McSween, H.Y., Bodnar, R.J., and Taylor,
282 L.A. (2013) The Tissint Martian meteorite as evidence for the largest impact excavation.
283 *Nature Communications*, 4, 1404.
- 284 Boehler, R., and De Hantsetters, K. (2004) New anvil designs in diamond-cells. *High Pressure*
285 *Research*, 24, 391–396.
- 286 Boyce, J.W., Tomlinson, S.M., McCubbin, F.M., Greenwood, J.P., and Treiman, A.H. (2014)
287 The lunar apatite paradox. *Science*, 344, 400–402.
- 288 Brunet, F., Allan, D.R., Redfern, S.A.T., Angel, R.J., Miletich, R., Reichmann, H.J., Sergent, J.,
289 and Hanfland, M. (1999) Compressibility and thermal expansivity of synthetic apatites,
290 $\text{Ca}_5(\text{PO}_4)_3\text{X}$ with X = OH, F and Cl. *European Journal of Mineralogy*, 11, 1023–1035.
- 291 Cámara, F., Curetti, N., Benna, P., Abdu, Y.A., Hawthorne, F.C., and Ferraris, C. (2018) The
292 effect of type-B carbonate content on the elasticity of fluorapatite. *Physics and Chemistry*
293 *of Minerals*, 45, 789–800.
- 294 Chen, M., Wopenka, B., Xie, X., and El Goresy, A. (1995) A new high-pressure polymorph of
295 chlorapatite in the shocked sixiangkou (L6) chondrite. Presented at the Lunar and
296 Planetary Science Conference XXVI, Abs#237.
- 297 Comodi, P., Liu, Y., Zanazzi, P.F., and Montagnoli, M. (2001) Structural and vibrational
298 behaviour of fluorapatite with pressure. Part I: in situ single-crystal X-ray diffraction
299 investigation. *Physics and Chemistry of Minerals*, 28, 219–224.

Revision 4

Word count: 3530

- 300 Cox, M.A., Erickson, T.M., Schmieder, M., Christoffersen, R., Ross, D.K., Cavosie, A.J., Bland,
301 P.A., Kring, D.A., and IODP–ICDP Expedition 364 Scientists (2020) High-resolution
302 microstructural and compositional analyses of shock deformed apatite from the peak ring
303 of the Chicxulub impact crater. *Meteoritics & Planetary Science*, 55, maps.13541.
- 304 Dong, Z., and White, T.J. (2004a) Calcium-lead fluoro-vanadinite apatites. I. Disequilibrium
305 structures. *Acta Crystallographica*, B60, 138–145.
- 306 ——— (2004b) Calcium-lead fluoro-vanadinite apatites. II. Equilibrium structures. *Acta*
307 *Crystallographica*, B60, 146–154.
- 308 Fei, Y., Ricolleau, A., Frank, M., Mibe, K., Shen, G., and Prakapenka, V. (2007) Toward an
309 internally consistent pressure scale. *Proceedings of the National Academy of Sciences*,
310 104, 9182–9186.
- 311 Hovis, G., Abraham, T., Hudacek, W., Wildermuth, S., Scott, B., Altomare, C., Medford, A.,
312 Conlon, M., Morris, M., Leaman, A., and others (2015) Thermal expansion of F-Cl
313 apatite crystalline solutions. *American Mineralogist*, 100, 1040–1046.
- 314 Hovis, G.L., Scott, B.T., Altomare, C.M., Leaman, A.R., Morris, M.D., Tomaino, G.P., and
315 McCubbin, F.M. (2014) Thermal expansion of fluorapatite-hydroxylapatite crystalline
316 solutions. *American Mineralogist*, 99, 2171–2175.
- 317 Hübschle, C.B., Sheldrick, G.M., and Dittrich, B. (2011) *ShelXle*: a Qt graphical user interface
318 for *SHELXL*. *Journal of Applied Crystallography*, 44, 1281–1284.
- 319 Hughes, J.M. (2015) The many facets of apatite. *American Mineralogist*, 100, 1033–1039.
- 320 Hughes, J.M., and Rakovan, J.F. (2015) Structurally Robust, Chemically Diverse: Apatite and
321 Apatite Supergroup Minerals. *Elements*, 11, 165–170.
- 322 Hughes, J.M., Cameron, M., and Crowley, K.D. (1989) Structural variations in natural F, OH,
323 and Cl apatites. *American Mineralogist*, 74, 870–876.
- 324 Hughes, J.M., Heffernan, K.M., Goldoff, B., and Nekvasil, H. (2014) Cl-rich fluorapatite devoid
325 of OH, from the Three Peaks area, Utah: The first reported structure of natural Cl-rich
326 fluorapatite. *The Canadian Mineralogist*, 52, 643–652.
- 327 Kenny, G.G., Karlsson, A., Schmieder, M., Whitehouse, M.J., Nemchin, A.A., and Bellucci, J.J.
328 (2020) Recrystallization and chemical changes in apatite in response to hypervelocity
329 impact. *Geology*, 48, 19–23.
- 330 Konzett, J., and Frost, D.J. (2009) The High P–T Stability of Hydroxyl-apatite in Natural and
331 Simplified MORB—an Experimental Study to 15 GPa with Implications for Transport
332 and Storage of Phosphorus and Halogens in Subduction Zones. *Journal of Petrology*, 50,
333 2043–2062.

Revision 4

Word count: 3530

- 334 Konzett, J., Rhede, D., and Frost, D.J. (2012) The high PT stability of apatite and Cl partitioning
335 between apatite and hydrous potassic phases in peridotite: an experimental study to 19
336 GPa with implications for the transport of P, Cl and K in the upper mantle. *Contributions*
337 *to Mineralogy and Petrology*, 163, 277–296.
- 338 Mao, H.K., Xu, J., and Bell, P.M. (1986) Calibration of the ruby pressure gauge to 800 kbar
339 under quasi-hydrostatic conditions. *Journal of Geophysical Research*, 91, 4673.
- 340 Matsukage, K.N., Ono, S., Kawamoto, T., and Kikegawa, T. (2004) The compressibility of a
341 natural apatite. *Physics and Chemistry of Minerals*, 31, 580–584.
- 342 McCubbin, F.M., and Jones, R.H. (2015) Extraterrestrial apatite: planetary geochemistry to
343 astrobiology. *Elements*, 11, 183–188.
- 344 McCubbin, F.M., Steele, A., Nekvasil, H., Schnieders, A., Rose, T., Fries, M., Carpenter, P.K.,
345 and Jolliff, B.L. (2010) Detection of structurally bound hydroxyl in fluorapatite from
346 Apollo Mare basalt 15058,128 using TOF-SIMS. *American Mineralogist*, 95, 1141–1150.
- 347 McCubbin, F.M., Jolliff, B.L., Nekvasil, H., Carpenter, P.K., Zeigler, R.A., Steele, A., Elardo,
348 S.M., and Lindsley, D.H. (2011) Fluorine and chlorine abundances in lunar apatite:
349 Implications for heterogeneous distributions of magmatic volatiles in the lunar interior.
350 *Geochimica et Cosmochimica Acta*, 75, 5073–5093.
- 351 Murayama, Nakai, S., Kato, M., and Kumazawa, M. (1986) A dense polymorph of $\text{Ca}_3(\text{PO}_4)_2$: a
352 high pressure phase of apatite decomposition and its geochemical significance. *Physics of*
353 *the Earth and Planetary Interiors*, 44, 293–303.
- 354 Palmer, D.C. (2015) Visualization and analysis of crystal structures using CrystalMaker
355 software. *Zeitschrift für Kristallographie-Crystalline Materials*, 230, 559–572.
- 356 Rivers, M., Prakapenka, V., Kubo, A., Pullins, C., Holl, C., and Jacobsen, S. (2008) The
357 COMPRES/GSECARS gas-loading system for diamond anvil cells at the Advanced
358 Photon Source. *High Pressure Research*, 28, 273–292.
- 359 Sarafian, A.R., Roden, M.F., and Patiño-Douce, A.E. (2013) The volatile content of Vesta: Clues
360 from apatite in eucrites. *Meteoritics & Planetary Science*, 48, 2135–2154.
- 361 Schouwink, P., Miletich, R., Ullrich, A., Glasmacher, U.A., Trautmann, C., Neumann, R., and
362 Kohn, B.P. (2010) Ion tracks in apatite at high pressures: the effect of crystallographic
363 track orientation on the elastic properties of fluorapatite under hydrostatic compression.
364 *Physics and Chemistry of Minerals*, 37, 371–387.
- 365 Sha, M.C., Li, Z., and Bradt, R.C. (1994) Single-crystal elastic constants of fluorapatite,
366 $\text{Ca}_5\text{F}(\text{PO}_4)_3$. *Journal of Applied Physics*, 75, 7784–7787.
- 367 Sheldrick, G. (2014) SHELXT: Integrating space group determination and structure solution.
368 *Acta Crystallographica Section A Foundations and Advances*, 70, C1437–C1437.

Revision 4

Word count: 3530

- 369 Shen, G., Wang, Y., Dewaele, A., Wu, C., Fratanduono, D.E., Eggert, J., Klotz, S., Dziubek,
370 K.F., Loubeyre, P., Fat'yanov, O.V., and others (2020) Toward an international practical
371 pressure scale: A proposal for an IPPS ruby gauge (IPPS-Ruby2020). High Pressure
372 Research, 40, 299–314.
- 373 Sudarsanan, K., and Young, R.A. (1978) Structural interactions of F, Cl and OH in apatites. Acta
374 Crystallographica, B34, 1401–1407.
- 375 Sugiyama, K., and Tokonami, M. (1987) Structure and crystal chemistry of a dense polymorph
376 of tricalcium phosphate $\text{Ca}_3(\text{PO}_4)_2$: A host to accommodate large lithophile elements in
377 the earth's mantle. Physics and Chemistry of Minerals, 15, 125–130.
- 378 White, T., Ferraris, C., Kim, J., and Madhavi, S. (2005) Apatite - an adaptive framework
379 structure. Reviews in Mineralogy and Geochemistry, 57, 307–401.
- 380 White, T.J., and Dong, Z. (2003) Structural derivation and crystal chemistry of apatites. Acta
381 Crystallographica, B59, 1–16.
- 382 Williams, Q., and Knittle, E. (1996) Infrared and raman spectra of $\text{Ca}_5(\text{PO}_4)_3\text{F}_2$ -fluorapatite at
383 high pressures: Compression-induced changes in phosphate site and Davydov splittings.
384 Journal of Physics and Chemistry of Solids, 57, 417–422.
- 385 Xia, X., Weidner, D.J., and Zhao, H. (1998) Equation of state of brucite: Single-crystal Brillouin
386 spectroscopy study and polycrystalline pressure-volume-temperature measurement.
387 American Mineralogist, 83, 68–74.
- 388 Xie, X., Zhai, S., Chen, M., and Yang, H. (2013) Tuite, $\gamma\text{-Ca}_3(\text{PO}_4)_2$, formed by chlorapatite
389 decomposition in a shock vein of the Suizhou L6 chondrite. Meteoritics & Planetary
390 Science, 48, 1515–1523.
- 391 Young, E.J., Myers, A.T., Munson, E.L., and Conklin, N.M. (1969) Mineralogy and
392 geochemistry of fluorapatite from Cerro de Mercado, Durango, Mexico. U.S. Geological
393 Survey Professional Papers, 650-D, D84–D93.
- 394 Zhang, D., Dera, P.K., Eng, P.J., Stubbs, J.E., Zhang, J.S., Prakapenka, V.B., and Rivers, M.L.
395 (2017) High pressure single crystal diffraction at PX^2 . Journal of Visualized
396 Experiments, 54660.

397 Figure Captions: (Figures added as separate files and included below)

398 **Figure 1.** Crystal structure of fluorapatite at ambient conditions. The Ca1, Ca2, P, and F ions are
399 represented as red, blue, yellow, and green spheres, respectively, with oxygen ions in grey. Fluorine
400 anions reside in channels parallel to the *c*-axis formed by Ca2 ions arranged in a triangle, indicated by the
401 dashed red lines. A unit cell is outlined by the solid black line.

402 **Figure 2.** Variation of fluorapatite unit cell parameters with pressure. Filled circles are from this study
403 (error bars are smaller than the symbol size when not shown) with previous single-crystal data as hollow
404 circles (Comodi et al., 2001). Dashed lines are fits to a linearized Burch-Murnaghan equation.

Revision 4

Word count: 3530

405 **Figure 3.** Variation of axial compressibilities of fluorapatite as a function of pressure from the fit to a
406 linearized Birch-Murnaghan equation.

407 **Figure 4.** Variation in the c/a ratio with pressure for fluorapatite. The present data, shown as filled
408 symbols (error bars are smaller than symbol size), are compared to previous studies by Comodi et al.
409 (2001) (hollow circles), Matsukage et al. (2004) (hollow triangles), and Brunet et al. (1999) (hollow
410 squares).

411 **Figure 5.** Volume versus pressure for fluorapatite together with a 3rd order Burch-Murnaghan fits to the
412 data.

413 **Figure 6.** Comparison of selected features of the crystal structures of FAp and FAp-II, at 25.8 GPa and
414 43.4 GPa, respectively.

415 **Figure 7.** Ca2' column configuration. F1A, F1B, and F1C indicate the positions of the three ideal fluorine
416 sites. F1A and F1B anions have half occupancy and oscillate between two locations. The Ca2'
417 configuration involves two 9 coordinated layers (X, and X') and two combined 8 and 9 coordinated layers
418 (Y and Y'). Ca ions are labeled with their letter designation, see Supplementary Table 3.

419 **Figure 8.** Volume per formula unit of apatite versus pressure. 3rd order Burch-Murnaghan equation of
420 state fits are shown for FAp (red) and FAp-II (black). The gray symbols indicate data for which the
421 quality of the refinement was poor. Arrow indicates datum collected on decompression from peak
422 pressure.

423 **Figure 9.** Variation of the average Ca-O bond lengths for anions bonded to Ca1 (a) and Ca2 (b) in FAp
424 with compression.

425 **Supplementary Figure 1.** Ambient Raman spectrum of [001]-oriented Durango apatite used in this study
426 (blue) compared with Durango apatite from the RRUFF database (red) (Lafuente et al., 2015). Data were
427 collected using a 532-nm laser, 20x objective, 30-second collection time with two accumulations, and a
428 600-gr/mm grating.

429 **Supplementary Figure 2.** Precession image showing measured reflections at 5.6 GPa in the $hk0$ plane
430 (top) and the same image with an expected reflection overlay (bottom). Precession images are calculated
431 in APEX3.

432 **Supplementary Figure 3.** The variation between the Ca1 site of FAp (left column) and the Ca1[8] site of
433 FAp-II (right column) is illustrated. The oxygen ions bonded to the Ca cations are colored such that
434 equivalent sites correspond across phases (top). The oxygen involved in the coordination change is
435 highlighted in pink (middle). The bonding environment of this oxygen is shown for each phase (bottom).

436

437

438

439

440

Revision 4
Word count: 3530

441

442

443

444

445

446

447

Table 1. Representative 300-K single-crystal structure refinements and refined atomic parameters for fluorapatite (Fap) at ambient pressure and 25.8 GPa.

Beamline	13-BM-C (PX ²), GSECARS, APS, ANL	
Pressure (GPa)	0.0001	25.8
Wavelength (Å)	0.4343	0.4343
Temperature (K)	295	295
Composition*	Ca ₅ (PO ₄) ₃ F	Ca ₅ (PO ₄) ₃ F
Symmetry	Hexagonal, P 6 ₃ /m	Hexagonal, P 6 ₃ /m
Lattice Parameters: <i>a</i> , <i>b</i> , <i>c</i> (Å)	See table 2	See table 2
Volume (Å ³)	See table 2	See table 2
Z	2	2
<i>R</i> _{int}	0.0495	0.0371
Reflection range	-14 ≤ <i>h</i> ≤ 14, -14 ≤ <i>k</i> ≤ 14, -10 ≤ <i>l</i> ≤ 10	-10 ≤ <i>h</i> ≤ 6, -8 ≤ <i>k</i> ≤ 8, -7 ≤ <i>l</i> ≤ 8
Maximum 2θ (°)	39	32.5
Total reflections collected	13459	1387
Independent reflections	718	414
Completeness	99.4 %	69.7 %
Number independent parameters	39	39
Refinement method	F ²	F ²
R1	0.0323	0.0363
wR2	0.0845	0.0932

Revision 4
 Word count: 3530

Goodness of fit		1.236	1.132		
Atom	Site occupancy	<i>x/a</i>	<i>y/b</i>	<i>z/c</i>	<i>U_{iso}</i>
<i>0.0001 GPa</i>					
Ca1	1	0.666667	0.333333	0.00108(6)	0.00630(14)
Ca2	1	0.99289(4)	0.24202(4)	0.25	0.00504(14)
P1	1	0.36902(5)	0.39845(5)	0.25	0.00220(14)
O1	1	0.48454(17)	0.32689(18)	0.25	0.0071(2)
O2	1	0.46649(18)	0.58795(17)	0.25	0.0090(3)
O3	1	0.25727(12)	0.34203(14)	0.07026(14)	0.0110(2)
F	0.5	0.0	0.0	0.25	0.0200(6)
<i>25.8 GPa</i>					
Ca1	1	0.666667	0.333333	0.99776(18)	0.0116(3)
Ca2	1	0.98258(10)	0.22328(11)	0.25	0.0062(2)
P1	1	0.37167(14)	0.39808(14)	0.25	0.0050(3)
O1	1	0.4854(4)	0.3144(4)	0.25	0.0119(6)
O2	1	0.4795(4)	0.5967(4)	0.25	0.0192(8)
O3	1	0.2537(3)	0.3412(4)	0.0636(5)	0.0236(7)
F	0.5	0.0	0.0	0.3990(17)	0.028(2)

*Nominal. The measured composition was (Ca_{5.05}Na_{0.04})(P_{2.93}Si_{0.03}S_{0.02}O₄)₃(F_{0.88}Cl_{0.06}OH_{0.04})

448

Tables:

449

450

451

452

453

454

455

456

457

458

Revision 4
 Word count: 3530

459
 460
 461
 462
 463
 464

465

Table 2. Unit cell parameters for fluorapatite (FAP).

Pressure (GPa)	<i>a</i> (Å)	<i>c</i> (Å)	Volume (Å ³)
Ambient	9.3937(4)	6.8821(3)	525.93(5) ⁴⁶⁶
0.5(1)	9.3768(5)	6.8755(6)	523.53(7) ⁴⁶⁷
2.9(1)	9.2892(5)	6.8342(5)	510.71(5)
5.6(1)	9.2059(5)	6.7930(5)	498.57(5) ⁴⁶⁸
8.3(1)	9.1290(5)	6.7532(5)	487.40(5)
10.3(1)	9.0972(4)	6.7425(4)	480.27(5) ⁴⁶⁹
12.6(1)	9.0214(3)	6.6940(5)	471.81(5)
15.4(1)	8.9584(3)	6.6560(5)	462.60(5) ⁴⁷⁰
19.4(2)	8.8736(3)	6.6016(5)	450.17(5)
22.7(1)	8.8132(5)	6.5589(5)	441.19(6)
25.8(1)	8.7588(3)	6.5171(5)	432.99(4) ⁴⁷¹
29.3(4)	8.7018(5)	6.4572(5)	423.44(6)
32.4(1.1)	8.6504(8)	6.3797(9)	413.4(1) ⁴⁷²

Error in pressure estimates were calculated through propagating the fit error of the [111] reflection to the final pressure. ⁴⁷³

Table 3. Burch-Murnaghan equation of state parameters

	<i>V</i> ₀ (Å ³)	<i>K</i> _{0T} (GPa)	<i>K'</i> _{0T}
<i>FAP</i>			
This study	525.93(5)*	95.8(4)	3.4(1)
	525.93(5)*	90.5**	4.1(1)
	525.93(5)*	92.3(5)	4*
Comodi et al., (2001)	524.23(5)	93(4)	5.8(1.8)

Revision 4
 Word count: 3530

474	Matsukage et al., (2004)	524.2(3)	91.5(38)	4.0(11)
		524.2(2)	91.6(10)	4*
475	Brunet et al., (1999)	522.2(4)	97.9(19)	4*
	FAP-II			
476	This study	258(9)	97(19)	4.1*
	* Fixed value.			
477	** K_{OT} (fixed) calculated from K_{OS} reported in Sha et al., (1994)			

478
 479
 480
 481
 482
 483

Table 4. Unit cell parameters for fluorapatite-II (FAP-II).

Pressure (GPa)	<i>a</i> (Å)	<i>b</i> (Å)	<i>c</i> (Å)	α (°)	β (°)	γ (°)	Volume (Å ³)
35.6(1.5)	8.636(3)	10.648(3)	10.7124(1)	88.407(9)	66.74(2)	66.62(1)	821.0(5)
38.6(1.7)	8.604(3)	10.591(4)	10.664(1)	88.39(1)	66.77(2)	66.62(2)	810.1(5)
41.4(1.7)	8.580(2)	10.534(3)	10.6251(7)	88.349(8)	66.85(2)	66.59(1)	801.0(4)
43.4*(1.7)	8.537(4)	10.536(4)	10.622(4)	88.361(5)	66.82(2)	66.54(1)	796.3(6)
44.7(1.8)	8.551(3)	10.479(4)	10.5765(9)	88.32(1)	66.93(2)	66.62(1)	791.4(5)
47.7(1.9)	8.525(2)	10.430(4)	10.533(8)	88.31(1)	67.01(2)	66.66(1)	782.8(5)
50.7(2.1)	8.497(2)	10.387(4)	10.4876(8)	88.313(9)	67.05(2)	66.68(1)	774.1(4)
53.5(1.8)	8.470(3)	10.345(9)	10.447(1)	88.31(2)	67.17(2)	66.72(2)	766.6(8)
55.7(3.0)	8.439(2)	10.305(3)	10.4046(7)	88.28(1)	67.16(2)	66.74(1)	758.0(4)
59.2(3.1)	8.419(2)	10.276(5)	10.3783(9)	88.224(9)	67.15(2)	66.75(1)	752.2(5)
61.0(2.1)	8.403(2)	10.254(4)	10.3536(8)	88.21(1)	67.17(2)	66.75(1)	747.5(5)

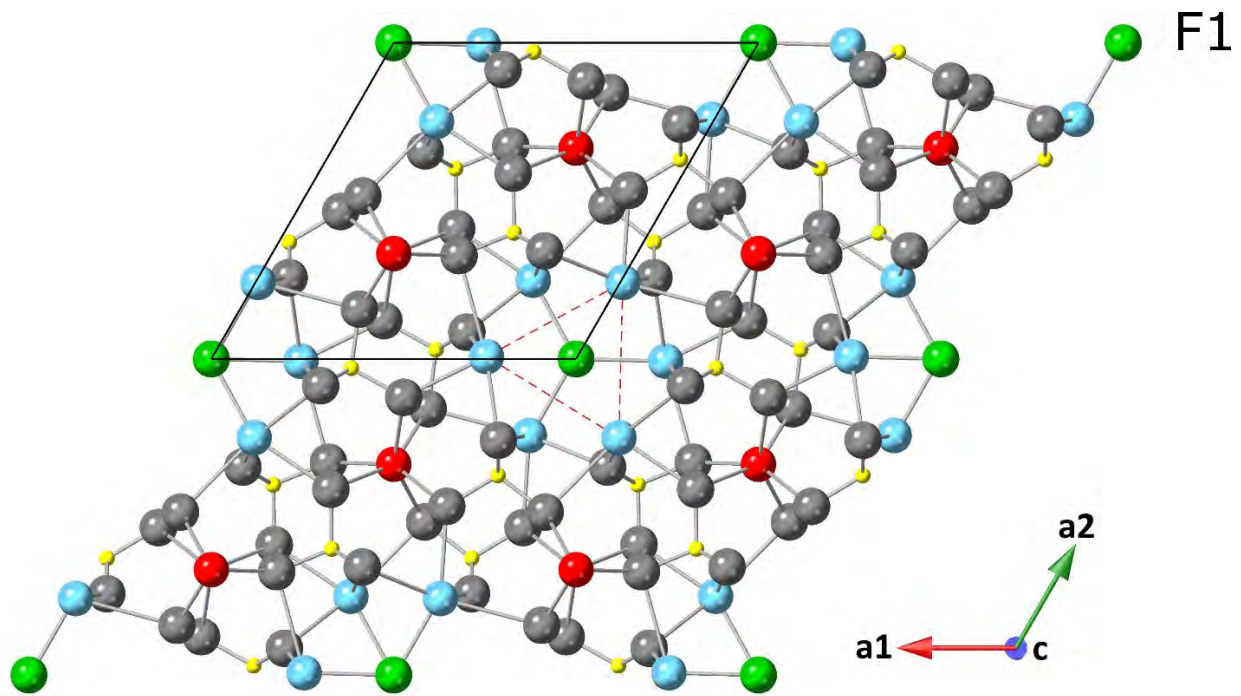
*Data at this pressure was used for the full structure refinement. Sample was partially decompressed from peak pressure (see text for details).

See footnote in Table 2 for pressure estimate description.

484
 485

Revision 4
Word count: 3530

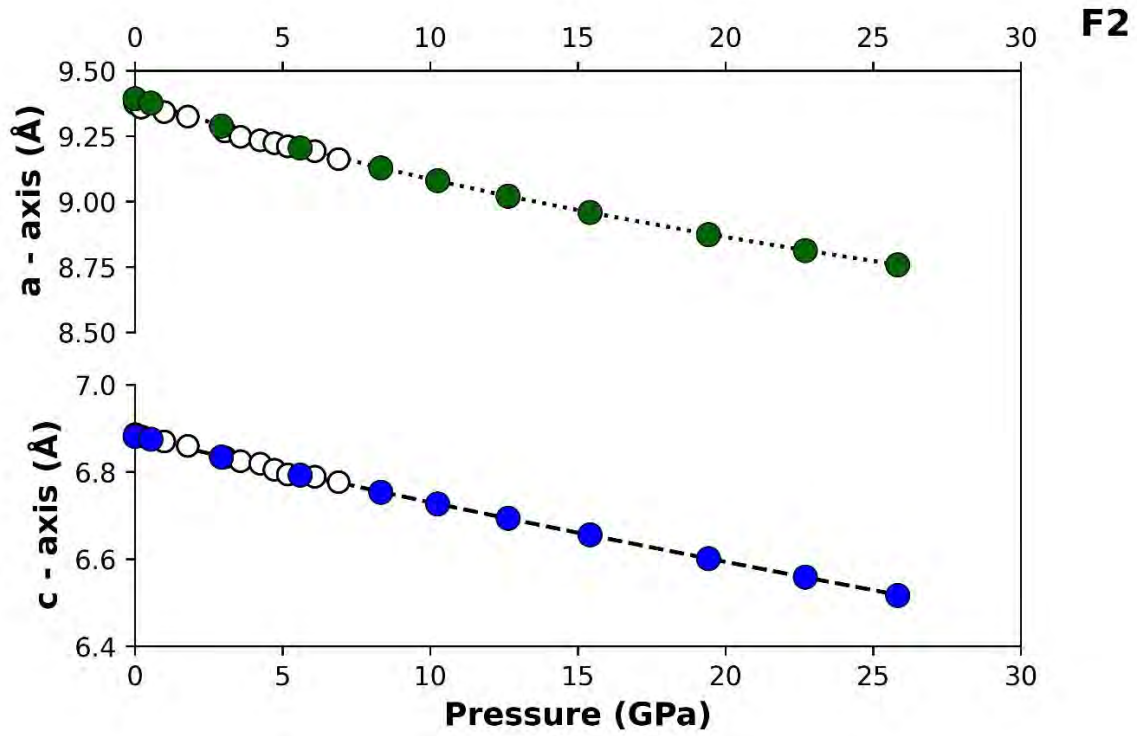
486
487
488
489
490
491
492
493
494
495
496



497

Revision 4
Word count: 3530

498



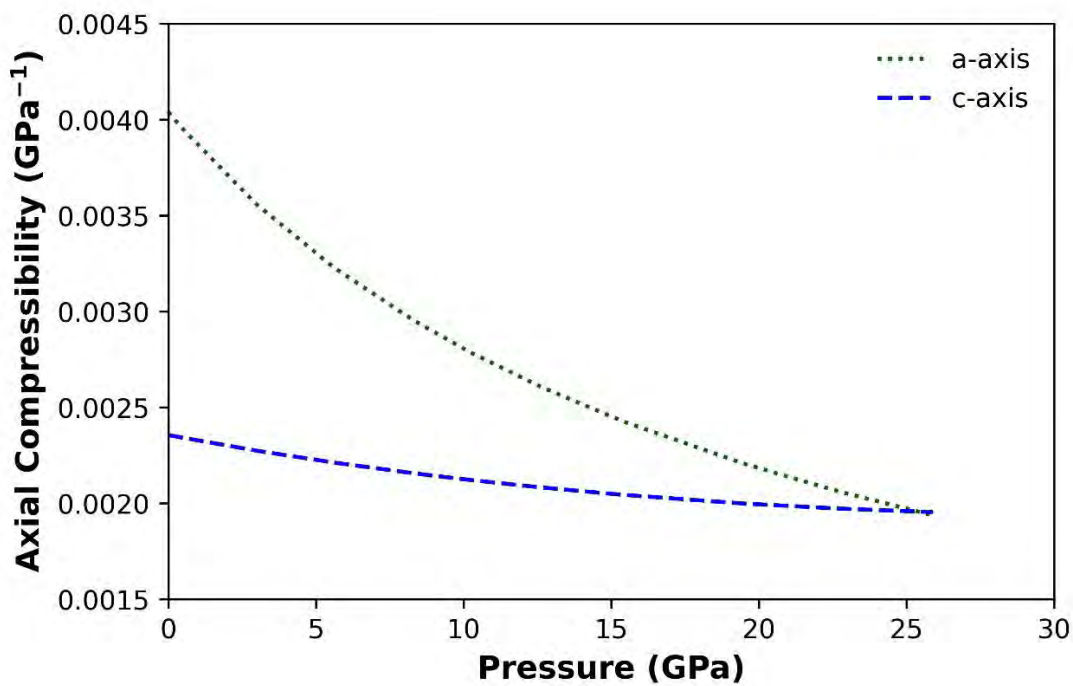
499

500

501

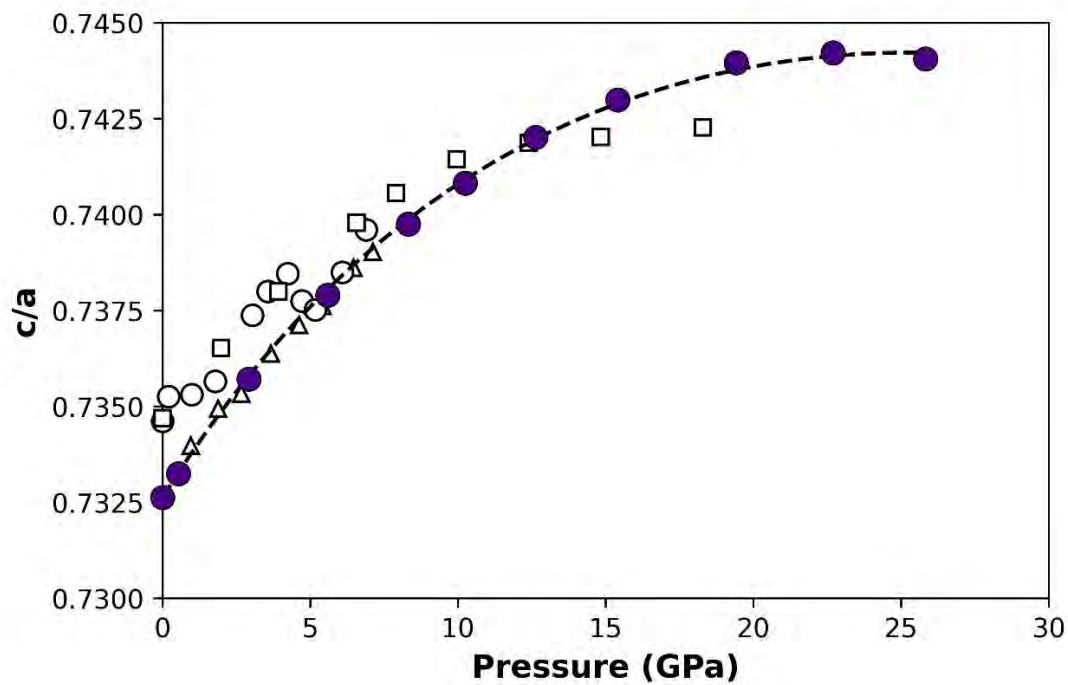
Revision 4
Word count: 3530

F3



502

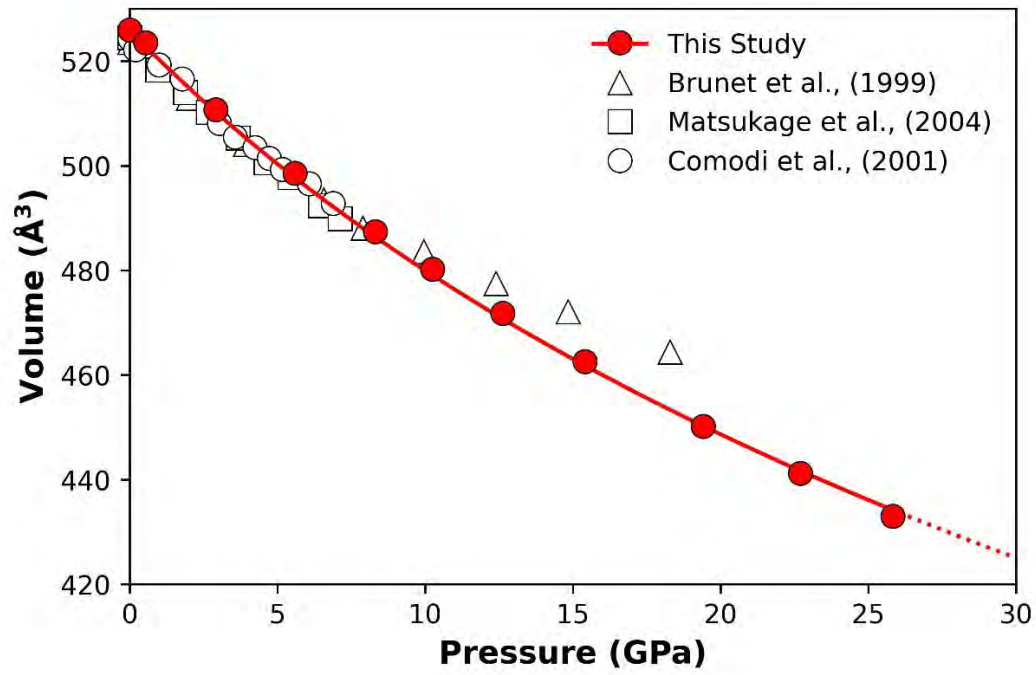
F4



503

Revision 4
Word count: 3530

F5

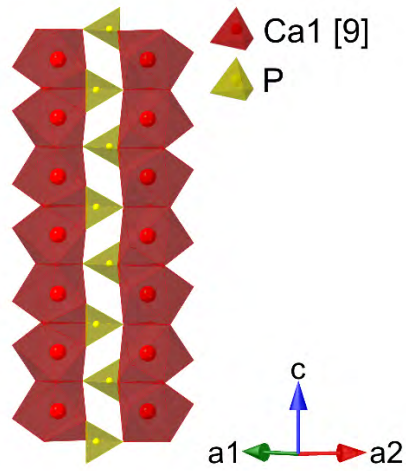


504

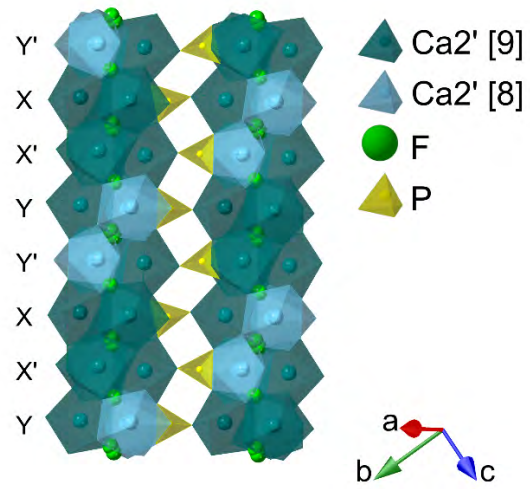
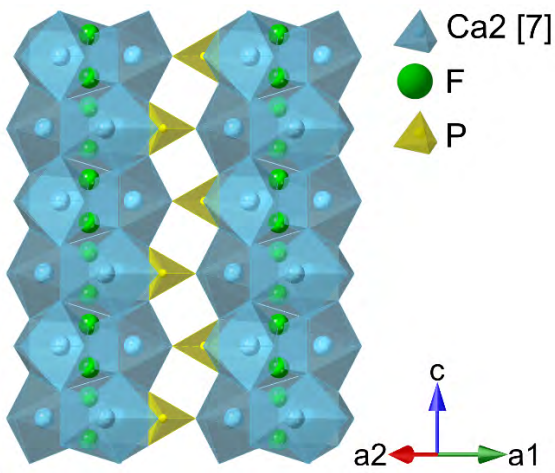
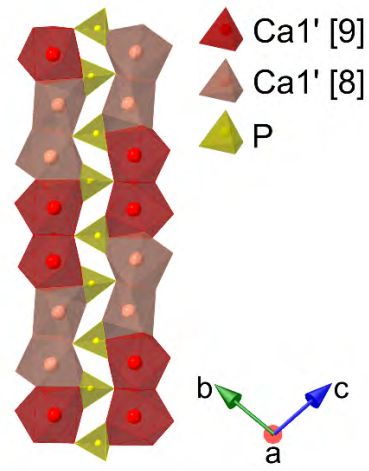
Revision 4
Word count: 3530

F6

**FAp
(25.8 GPa)**

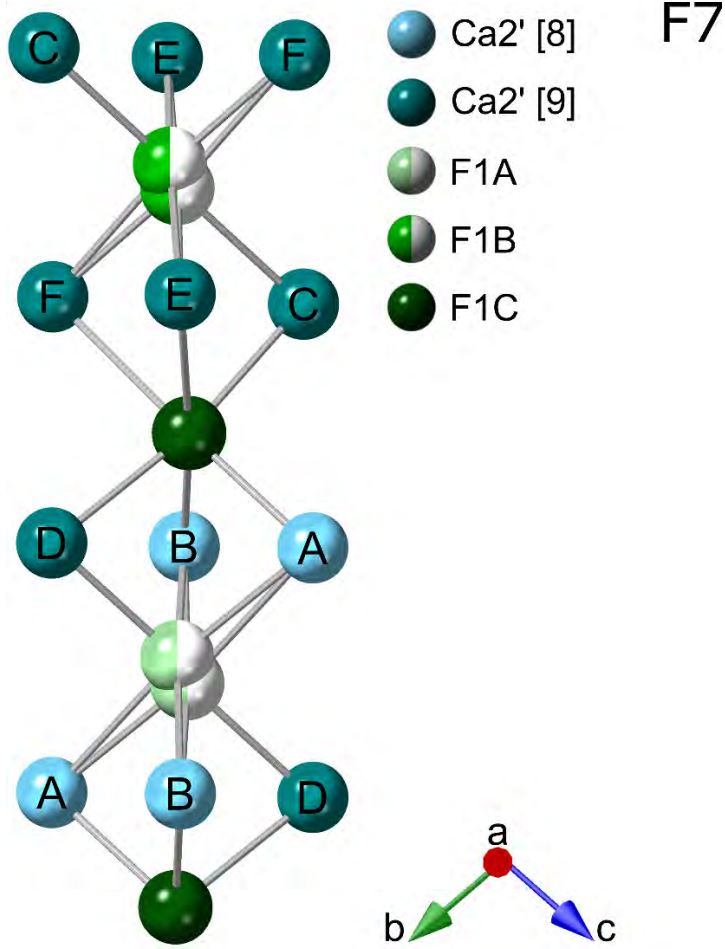


**FAp-II
(43.4 GPa)**



505

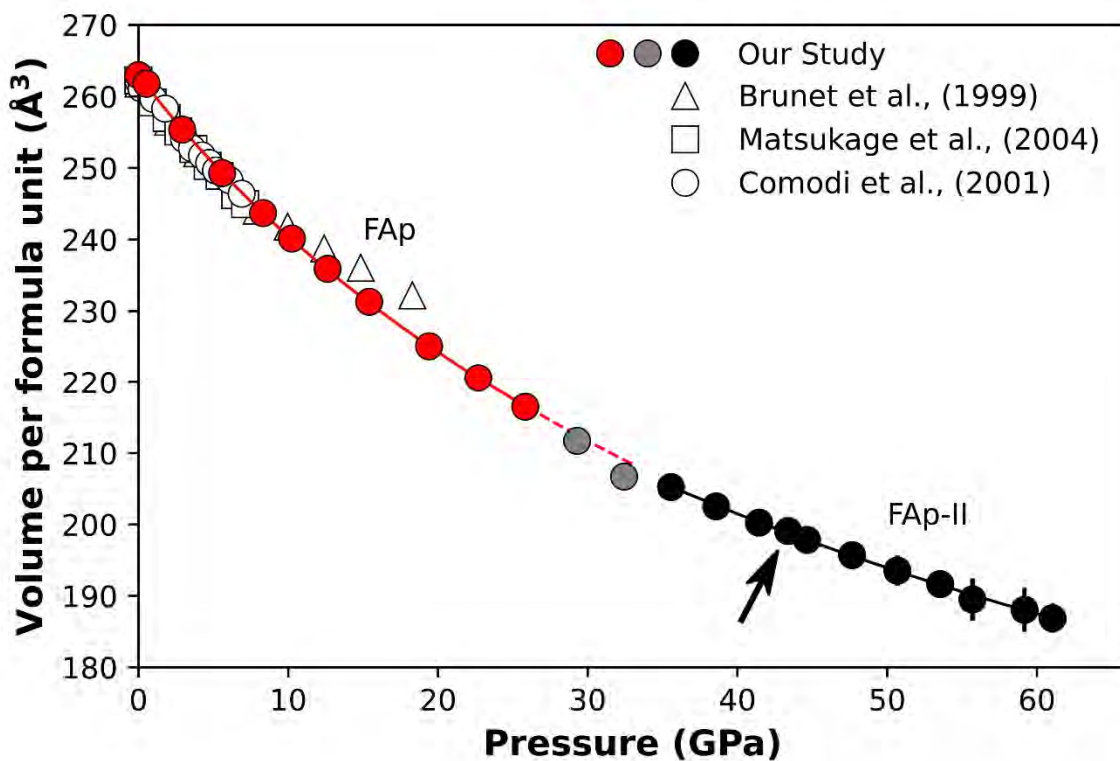
Revision 4
Word count: 3530



506

Revision 4
Word count: 3530

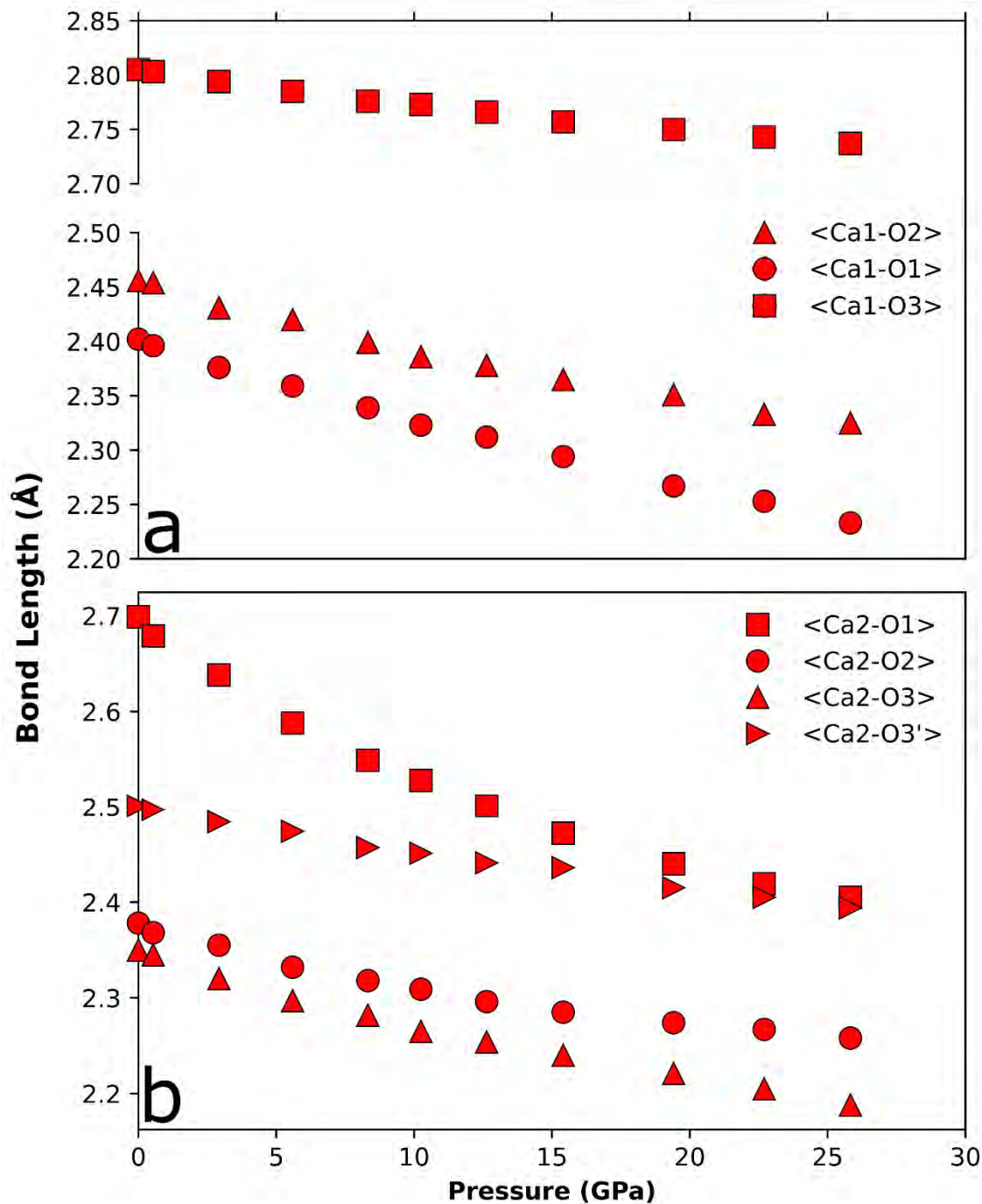
F8



507

Revision 4
Word count: 3530

F9



508
509
510
511
512